Nano Research

Open Access

Research Article

Membrane-disrupting saponin-polyphenols as tumor nanovaccine via immunogenic cell death and antigen capture

Baoli Ma[1,2], Jingsong Lu[3,4] ✉, Haimiti Aishanjiang[2], Jing Yu[3,4], Shenglei Che[3,4], Yen Wei[1] ✉, and Lingyun Zhao[2] ✉

[1] *The Key Laboratory of Bioorganic Phosphorus Chemistry & Chemical Biology (Ministry of Education), Department of Chemistry, Tsinghua University, Beijing 100084, China*
[2] *School of Materials Science and Engineering, Tsinghua University, Beijing 100084, China*
[3] *College of Materials Science and Engineering, Zhejiang University of Technology, Hangzhou 310014, China*
[4] *Research Center of Magnetic and Electronic Materials, Zhejiang University of Technology, Hangzhou 310014, China*

Cite this article: *Nano Research*, **2026**, *19*, 94908614. https://doi.org/10.26599/NR.2026.94908614

ABSTRACT: Converting localized tumor destruction into systemic antitumor immunity remains a central challenge in cancer immunotherapy. In this study, we present a rationally designed antigen-capturing nanoplatform composed of tannic acid (TA) and saponin, which self-assemble to encapsulate photosensitizer, forming saponin-polyphenol nanoparticles (ISNPs) with multifunctional immunotherapeutic potential. Leveraging the membrane-perturbing properties of saponin, ISNPs induce acute plasma membrane disruption and promote the release of damage-associated molecular patterns (DAMPs), such as calreticulin (CRT) and high-mobility group box 1 (HMGB1), thereby initiating immunogenic cell death (ICD) and supporting subsequent immune activation. Simultaneously, ISNPs induce nuclear membrane rupture and cytosolic DNA leakage. Notably, the polyphenol-rich surface of ISNPs enables efficient adsorption of tumor-associated antigens (TAAs), forming antigen–nanocomplexes that prolong antigen retention and facilitate dendritic cell (DC) uptake. In bilateral tumor-bearing mouse models, ISNP-mediated photothermal treatment not only eradicates primary tumors but also elicits a modest abscopal trend on distant lesions, marked by enhanced DC maturation and cytotoxic T lymphocyte infiltration. This work establishes a membrane-interfering, antigen-capturing nanoagent that effectively bridges local photothermal ablation and systemic immune activation, offering a promising strategy for *in situ* nanovaccination and personalized cancer immunotherapy.

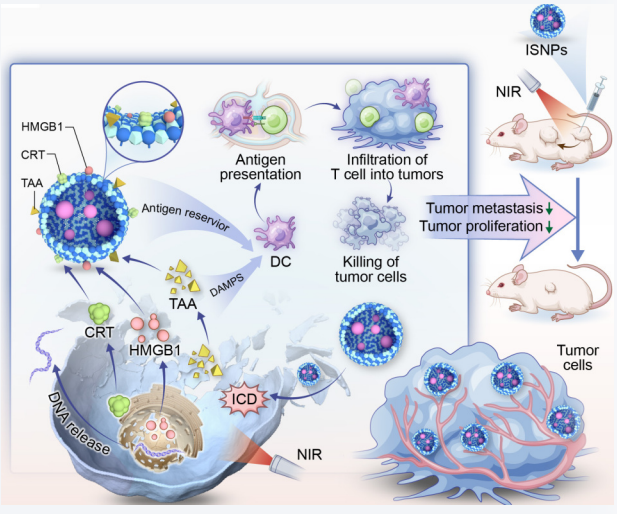

KEYWORDS: photothermal therapy, immunogenic cell death, antigen capture, saponin, polyphenol

1 Introduction

Saponins (amphipathic glycosides, SAP) are amphiphilic glycosides abundantly found in many plants with recognized adjuvant and membrane-permeabilizing properties [1, 2]. One such saponin, QS-21, is a purified saponin component that has been included in the licensed vaccine Shingrix™ due to its ability to enhance uptake of antigen by macrophages or dendritic cells (DCs) and T-cell priming [3, 4]. Mechanistically, saponins act through interaction with cholesterol-rich lipid membranes causing membrane disruption and the release of pro-inflammatory cytokines to facilitate the activation and migration of dendritic cells. Recent work, including our previous studies, shows that saponins could induce localized membrane disruption and trigger the release of intracellular substances [5–7], which are also known as damage-associated molecular patterns (DAMPs), containing adenosine triphosphate (ATP), calreticulin (CRT), and high-mobility group box 1 (HMGB1). However, this manner of immunogenic cell death (ICD)-like is often limited in some solid tumors due to the rapid metabolism of immunogenic substances and the existing immune suppressive microenvironment [8–10].

Received: December 15, 2025; **Revised:** February 28, 2026
Accepted: March 2, 2026

✉Address correspondence to Jingsong Lu, lujingsong@zjut.edu.cn; Yen Wei, weiyen@tsinghua.edu.cn; Lingyun Zhao, lyzhao@mail.tsinghua.edu.cn

To overcome these problems, *in situ* cancer vaccine has emerged as an important part of immunotherapy [11–13]. Usually, *in situ* vaccine uses naturally occurring tumor debris as the source of self-generated antigen, distinguished from conventional vaccine using known extracted tumor antigens [14–16]. It has been established that this process enables the circumvention of a predetermined antigen target and the generation of patient-specific immunity [17]. Despite the existence of optimal theoretical concepts pertaining to *in situ* vaccination, its practical efficacy remains challenging, arising from the rapid diffusion and proteolysis of tumor-associated antigens (TAAs) upon their release, which hinders their detection by antigen-presenting cells (APCs) [18–20]. The absence of any intrinsic property in the natural tumor milieu that stabilizes the antigenic structure, or functionality renders these antigens ineffective in eliciting an effective antitumor immune response. Nowadays, antigen-capturing nanomaterials have been developed to rapidly capture TAAs and facilitate antigen presentation [21, 22]. These substances are expected to quickly absorb TAAs following cell disruption, forming stable nanocomplexes that are resistant to enzymatic disintegration and promote lymphatic drainage [23, 24]. They also improve the rate of uptake by professional APCs. Among the many different classes of materials, polyphenol-based nanostructures, especially those constructed using tannic acid (TA), demonstrate superior antigen-binding capabilities [25–27]. TA has many galloyl groups that can form various non-covalent interactions with proteins, including hydrogen bonding, hydrophobic interactions and π–π stacking, which enables TA to act as a molecular glue, immobilizing TAAs onto the surface of nanoparticles to form stable, proteolysis-resistant antigen-nanocomplexes under physiological conditions [23, 28–31].

In this work, we present the construction of photosensitizer loaded indocyanine green (ICG) saponin-polyphenol nanoparticles (ISNPs) via the self-assembly of saponin and tannic acid as potential tumor vaccines and the investigation of the mechanism between membrane disruption and antitumor immunotherapy. ISNPs can alter cell membrane permeability and even disrupt these "membranes" structure directly, thereby facilitating the release of intracellular substances, including tumor-associated antigens, HMGB1, and CRT, under near-infrared (NIR) laser irradiation. Furthermore, these ISNPs also demonstrated the ability to disrupt the nuclear envelope, promoting the leakage of nuclear DNA into the cytosol, a phenomenon which may trigger the activation of the cyclic GMP-AMP synthase–stimulator of interferon genes (cGAS-STING) pathway and contribute to a pro-inflammatory immune response via boosting the type I interferon signal. Subsequently, the released TAAs would be effectively captured by ISNPs and formed antigen-captured nanocomplexes as an antigen reservoir. These effects promoted the recruitment of dendritic cells and stimulated immune effector responses (Scheme 1). Therefore, this nanovaccine strategy, focused on plasma membrane disruption and *in situ* antigen capture, represents a promising approach to augment ICD and enhance the efficacy of cancer immunotherapy.

2 Results and discussion

2.1 Preparation and characterization of tannic-acid–saponin nanoparticles (SNPs)

Fourier-transform infrared (FTIR) spectra of TA, SAP, and SNPs (Fig. 1(a)) displayed pronounced shifts in O–H stretching and carbonyl-associated bands after assembly, supporting the formation of extensive hydrogen-bonding interactions between the components. Given the polyphenol–glycoside nature of this noncovalently assembled scaffold, the SNPs can be considered a supramolecular co-assembly of tannic acid and saponin. The morphology and structure of the assembled nanoparticles were then examined by transmission electron microscopy (TEM). TEM images showed that the tannic acid–SNPs were overall well-dispersed and exhibited predominantly spherical morphologies (Fig. 1(b)). Occasional irregular outlines and dark electron-dense domains observed in TEM are likely attributable to local densification of the polyphenol-rich network and/or partial collapse during sample drying, which enhances contrast in higher-density regions, rather than uncontrolled aggregation in suspension. Dynamic light scattering (DLS) measurements showed a monomodal hydrodynamic size distribution with a mean diameter of approximately 141.8 nm (Fig. 1(c)). Zeta potential measurements from three independent runs indicated that SNPs exhibited a near-neutral, slightly negative surface potential (−6.27 ± 0.90 mV, n = 3; Fig. 1(d)), consistent with good colloidal dispersibility in aqueous media.

To test the cytocompatibility of SNPs, viability assays were performed upon 4T1 cells that were treated with the SNPs (Fig. 1(e)). Cell viability remained comparable to the untreated control at low concentrations (≤ 0.15 mg·mL^{-1}), whereas a pronounced transition occurred within a narrow window (~ 0.18–0.20 mg·mL^{-1}), consistent with a threshold-like onset of saponin-associated membrane stress. To resolve the transition region, we repeated the assay using a finer concentration spacing and provided the expanded dataset in Fig. S1 in the Electronic Supplementary Material (ESM). Using brightfield imaging, the direct acute membrane response of cells to these substances was detected post-treatment with 5 mg·mL^{-1} SAP and 2 mg·mL^{-1} SNPs (Fig. 1(f)). Importantly, a similar time-dependent membrane-perturbation trend was also observed at a lower concentration (0.5 mg·mL^{-1}), as shown in Fig. S2 in the ESM. In both treatments, there was an observable rapid collapse of cells within 30–90 s, evidenced by pronounced shrinkage, rounding and loss of membrane integrity. The response was more synchronous and faster during treatment with SNPs. Collectively, these results are commensurate with the long known cholesterol-dependent membrane-permeabilizing activity of saponins which collapse lipid packing, promote transient pore formation and ultimately lead to membrane disintegration [32].

2.2 Construction and characterization of ICG-loaded nanoparticles (ISNPs)

To gain an assembly with a photothermal function while preserving the membrane-disruptive behavior of SNPs, ICG was loaded into this system and the final product was called ISNPs. As can be seen, the UV–vis spectrum exhibits a strong NIR absorption with a maximum around 800 nm (Fig. 2(a)). Compared to free ICG, the peak is slightly red-shifted and somewhat broadened. This slight shift indicates that the dye is accommodated in a more restricted microenvironment within the TA–SAP network than it is when freely solvated in water, consistent with supramolecular confinement. Also supporting this interpretation, FTIR spectra again largely preserve the characteristic signatures of both TA and saponin, but with additional ICG-related bands without disrupting the primary hydrogen-bonded framework (Fig. 2(b)).

Dynamic characterization indicated further structural perturbation following ICG loading. Hydrodynamic diameters of

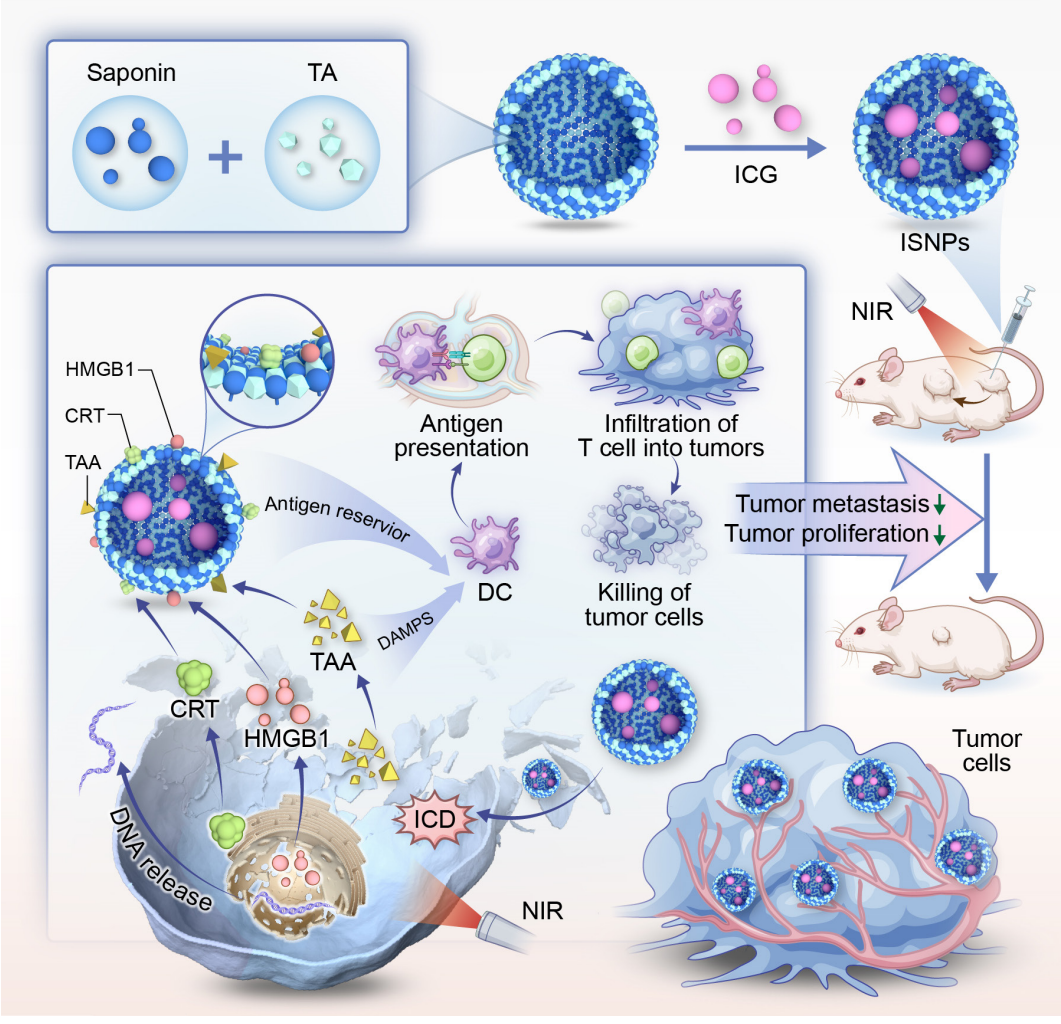

Scheme 1 Schematic illustration of the design and mechanism of ISNPs for *in situ* cancer vaccination. Saponin and TA self-assemble to form stable nanostructures that encapsulate the photothermal agent ICG, generating ISNPs. ISNPs disrupt the plasma and nuclear membranes of tumour cells and lead to the release of TAAs and DAMPs, such as CRT and HMGB1. The released TAAs are efficiently captured by the polyphenol-rich surface of the ISNPs to form antigen–nanocomplexes that act as an antigen reservoir. These nanocomplexes facilitate DC uptake and antigen presentation, promoting CTL infiltration into tumors and ultimately suppressing tumor growth.

unloaded SNPs were ~ 142 nm whereas ISNPs were slightly smaller ~ 120 nm, although they remained monodisperse (Fig. 2(d)). Zeta potentials measured from three independent runs showed that both SNPs and ICG-loaded ISNPs exhibited near-neutral, slightly negative surface potentials (ISNPs: −6.79 ± 0.38 mV; n = 3) (Fig. 2(c)). These data indicate that ICG loading does not induce a net charge inversion; instead, ICG incorporation is consistent with noncovalent association within the TA–saponin network (e.g., hydrophobic/π–π interactions and hydrogen bonding) and charge screening/compensation at the particle–medium interface [33]. Encapsulation efficiency (EE) and drug loading (DL) were determined to be 28.48% and 0.08% (ICG mass/particle mass, w/w), respectively, suggesting that a measurable fraction of the dye remains entrapped within the nanostructure (Fig. 2(e)) [34, 35].

We evaluated the *in vitro* cytocompatibility of ISNPs under dark conditions using CCK-8 assays (Fig. 2(f)) and further examined cytocompatibility toward primary immune cells using splenocytes as a mixed immune-cell population (Fig. S3 in the ESM). In parallel, lactate dehydrogenase (LDH) assays provided an orthogonal readout of membrane integrity by quantifying extracellular LDH released into the culture supernatant as a direct indicator of plasma membrane leakage. As shown in Fig. 2(h), ISNPs induced a dose-dependent increase in LDH release under dark conditions (100 and 200 μg·mL^{-1}), while near-infrared irradiation further enhanced LDH release at 200 μg·mL^{-1}, consistent with exacerbated membrane disruption following photothermal activation. Collectively, these results indicate that the TA–SAP scaffold retains membrane-disrupting activity after ICG loading, and photothermal treatment further amplifies membrane damage.

Finally, the intracellular distribution of the dye was investigated by confocal microscopy. Free ICG showed weak and heterogeneous fluorescence, due to its poor uptake and inefficient stability, whilst ISNPs-treated cells exhibited strong and homogeneous cytoplasmic fluorescence (Fig. 2(g)), indicating nanoscale-enabled cellular uptake. Together, these data show that ICG loading leads to alterations in the optical and surface properties of the TA–SAP assembly, leading to nanoscale particles with stable NIR absorption, a near-neutral surface potential, dose-dependent cytocompatibility under dark conditions, and improved intracellular delivery of ICG, which are important to their ensuing photothermal behavior [36].

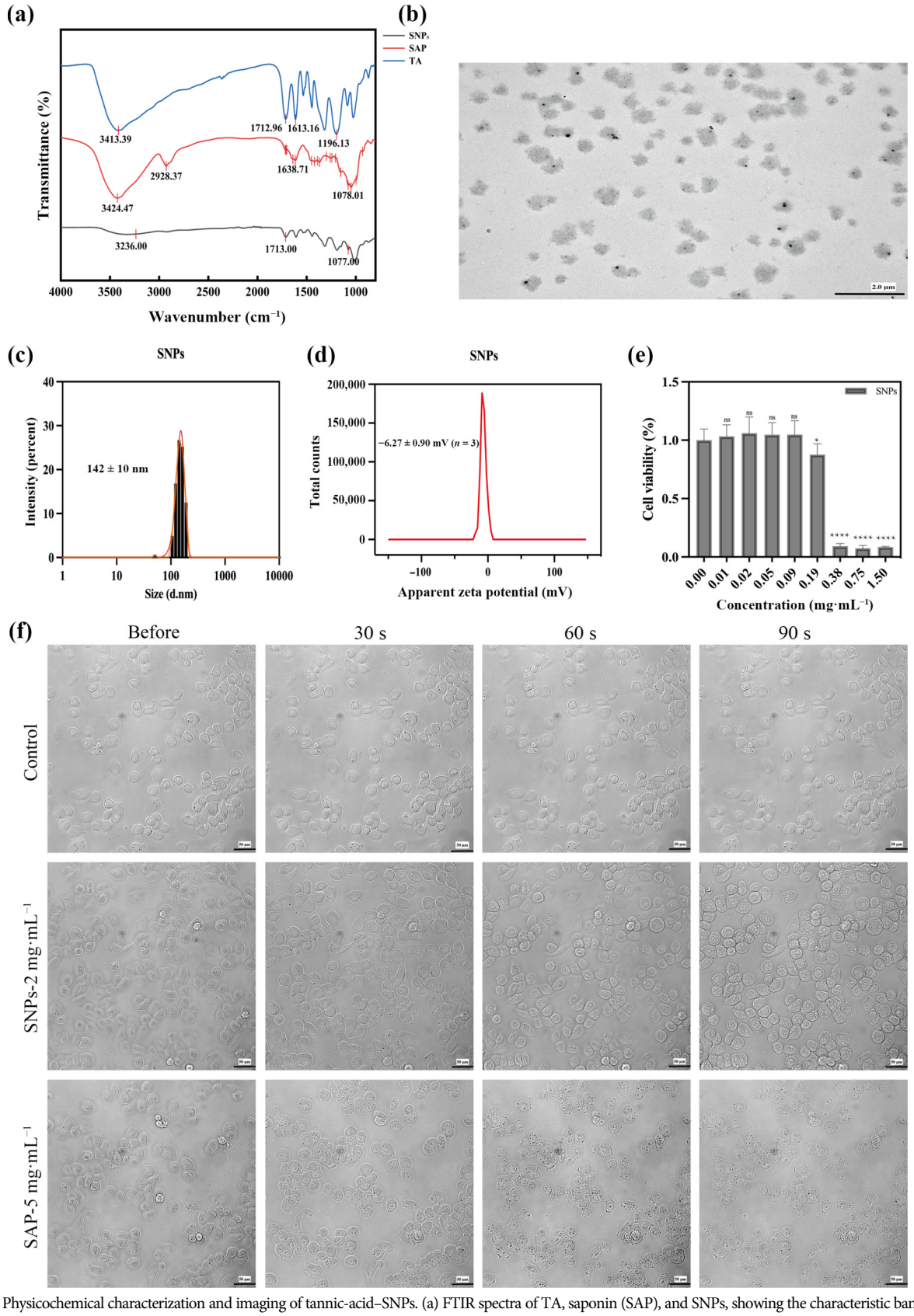

Figure 1 Physicochemical characterization and imaging of tannic-acid–SNPs. (a) FTIR spectra of TA, saponin (SAP), and SNPs, showing the characteristic bands of each component and the spectral changes following nanoparticle formation. (b) TEM image of SNPs with predominantly spherical morphology. Scale bar, 2 μm. (c) DLS size distribution of SNPs, with a hydrodynamic diameter centered around 142 nm. (d) Zeta potential distribution of SNPs (−6.27 ± 0.90 mV, n = 3). (e) CCK-8 assay of 4T1 cells incubated with SNPs (0–1.5 mg·mL^{-1}) for 24 h, showing cell viability. (f) Bright-field images of 4T1 cells recorded 30, 60, and 90 s after exposure to 5 mg·mL^{-1} SAP or 2 mg·mL^{-1} SNPs. Scale bars: 50 μm.

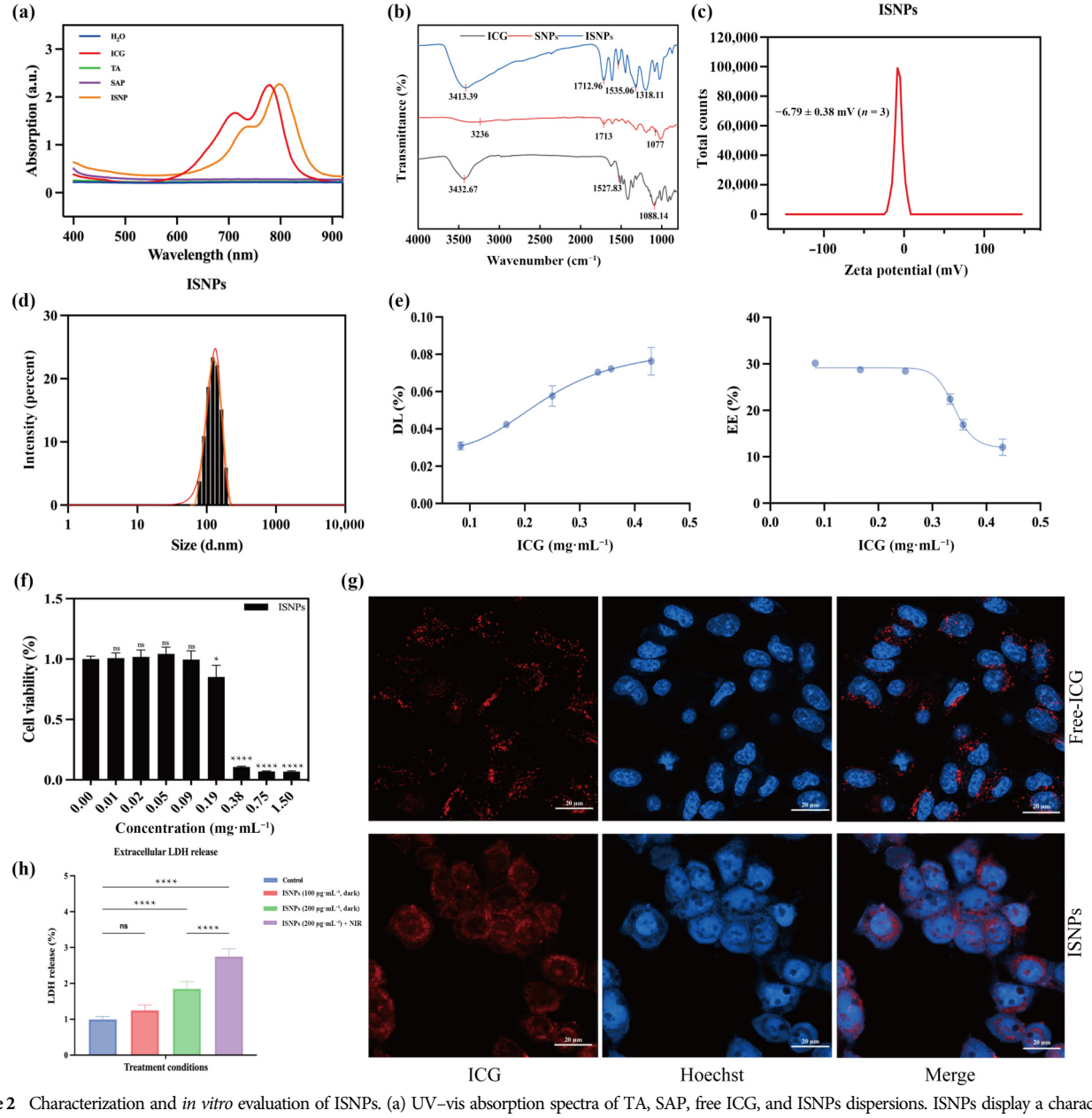

Figure 2 Characterization and *in vitro* evaluation of ISNPs. (a) UV–vis absorption spectra of TA, SAP, free ICG, and ISNPs dispersions. ISNPs display a characteristic NIR absorption band distinct from free ICG. (b) FTIR spectra of ICG, SNPs, and ISNPs, showing the preserved characteristic bands of SNPs and the additional ICG-associated vibrational features after loading. (c) Zeta potential distribution of ISNPs (−6.79 ± 0.38 mV, n = 3). (d) DLS size distribution of ISNPs, showing nanoscale hydrodynamic diameters with a narrow peak profile. (e) Encapsulation efficiency and loading content of ICG in ISNPs determined from the calibration curve (EE = 28.48%; DL = 0.08%). (f) Viability of 4T1 cells after 24 h incubation with increasing concentrations of ISNPs under dark conditions, quantified using the CCK-8 assay. (g) Confocal fluorescence microscopy images of 4T1 cells exposed to free ICG or ISNPs for 1 h. Red: ICG fluorescence; blue: Hoechst-stained nuclei. Scale bars: 20 μm. (h) Extracellular LDH release from 4T1 cells after incubation with ISNPs (100 or 200 μg·mL^{-1}, dark) or ISNPs (200 μg·mL^{-1}) plus NIR irradiation. Data are mean ± SD (n = 4). Statistical analysis was performed using one-way ANOVA with Tukey's multiple-comparison test.

2.3 *In vitro* photothermal performance, protein corona formation and photothermal cytotoxicity of ISNPs

The photothermal effects of ISNPs were probed using 808 nm irradiation. For a given concentration of nanoparticles, ISNPs dispersions showed a rapid and sustained increase in temperature while SNPs barely produced any heating (Fig. 3(a)). The degree of heating reflected the dye loading: higher formulation of ICG led to plateau temperatures of ~ 50–55 °C within 5 min (Fig. 3(b)) and simply increasing laser power density at a fixed ISNPs dose led to an elevated terminal temperature of ~ 65 °C under the strongest irradiation (Fig. 3(c)). Infrared thermal imaging qualitatively confirmed these trends, showing the localization of heating via time-dependent behavior of heating in ISNPs dispersions, while SNPs generally remained close to baseline (Fig. 3(f)). ISNPs also maintained stable photothermal performance after repeated irradiation. Five heating–cooling cycles generated nearly overlapping temperature profiles with no apparent decrease in peak temperature (Fig. 3(d)), confirming that the encapsulated ICG maintained its photothermal efficacy without obvious photobleaching or aggregation, common for free NIR dyes.

To assess the antigen-capturing property of ISNPs, a bovine

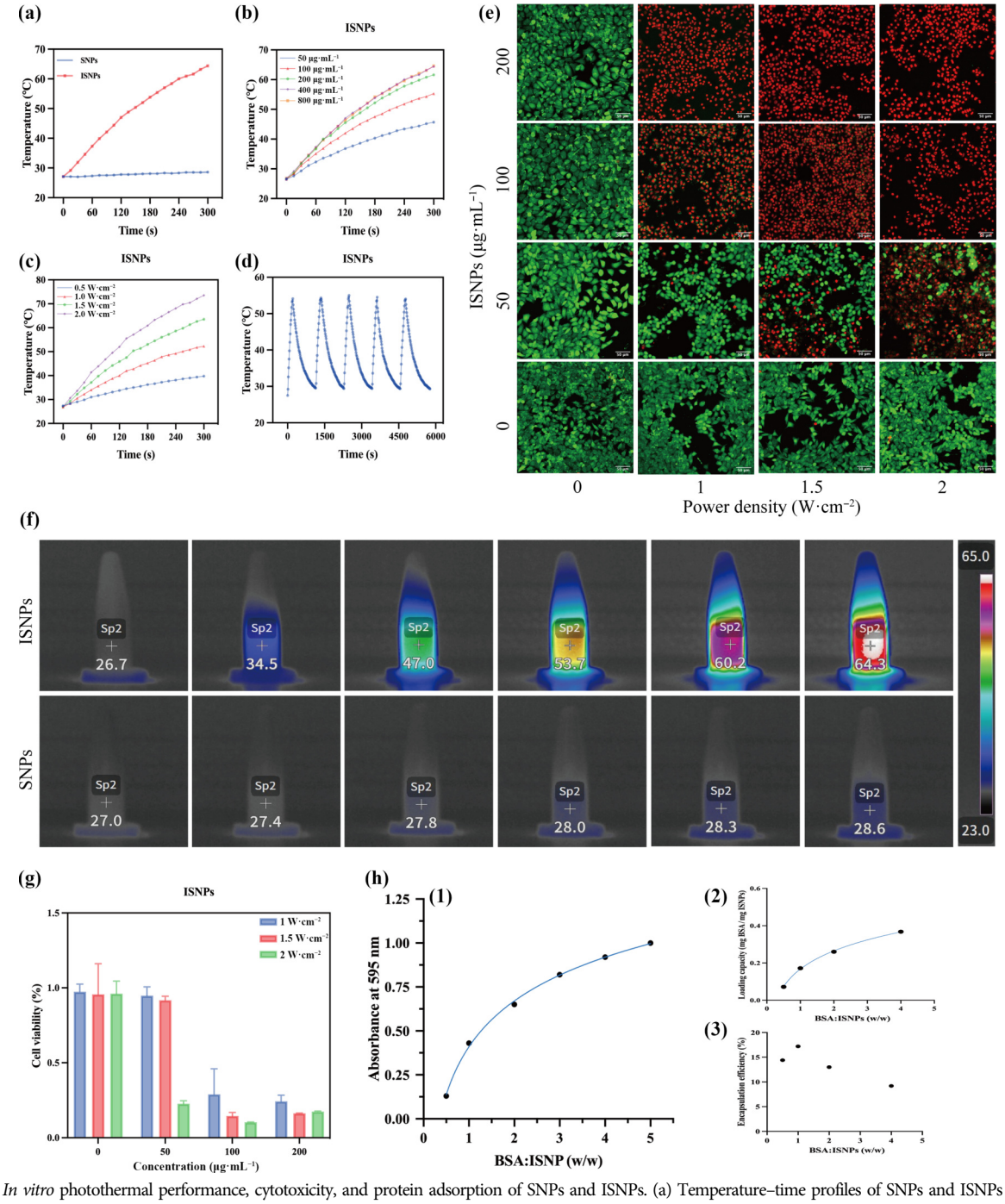

Figure 3 *In vitro* photothermal performance, cytotoxicity, and protein adsorption of SNPs and ISNPs. (a) Temperature–time profiles of SNPs and ISNPs dispersions under 808 nm laser irradiation at equal nanoparticle concentrations. (b) Photothermal heating behavior of ISNPs dispersions containing different ICG loadings under 808 nm irradiation. (c) Temperature evolution of ISNPs dispersions irradiated with 808 nm laser at varying power densities. (d) Photothermal cycling stability of ISNPs over five consecutive heating–cooling cycles under repeated 808 nm irradiation. (e) Confocal laser scanning microscopy images of 4T1 cells stained with Annexin V–FITC and PI after treatments with SNPs or ISNPs, with or without 808 nm irradiation. Scale bars: 50 μm. (f) Infrared thermal images of SNPs and ISNPs dispersions captured at designated time points during 808 nm irradiation. (g) Viability of 4T1 cells incubated with SNPs or ISNPs at different concentrations and irradiated at indicated laser power densities, assessed by the CCK-8 assay. (h) Protein adsorption on ISNPs: (1) BSA adsorption isotherm quantified by Bradford assay (A595) versus BSA-to-ISNP ratio, with the derived (2) loading capacity (mg BSA per mg ISNP) and (3) encapsulation efficiency (%); raw values are provided in Table S1 in the ESM.

serum albumin (BSA) adsorption assay was performed by quantifying the residual free BSA in the supernatant via absorbance at 595 nm. ISNPs exhibited strong, ratio-dependent BSA binding with a clear saturation behavior (Fig. 3(h)(1)). The corresponding loading capacity and encapsulation efficiency are summarized in Figs. 3(h)(2) and 3(h)(3), and the underlying values are provided in Table S1 in the ESM. The affinity of the ISNPs for proteins is consistent with the polyphenol-rich interface of TA-based nanostructures that benefit from strong noncovalent interaction to protein substrates via hydrogen bonding or π–π stacking between the phenolic groups and exposed residues. Functionally, this could mean that ISNPs could function as effective scavengers of TAAs

that become available upon damage to the tumor cell from saponin-mediated membrane disruption and from the subsequent photothermal killing. By binding to antigens as nano-complexes, ISNPs may increase local antigen retention and availability, which could potentially support antigen uptake by antigen-presenting cells and subsequent immune activation [37].

These physicochemical properties were then studied as parameters for cellular responses. In the absence of irradiation, both SNPs and ISNPs only produced a modest change in metabolism and viability was maintained above approximately 80% (Fig. 3(g), dark groups); in contrast upon exposure to NIR, ISNPs led to a dramatic and dose-dependent decrease in viability whereas irradiation had negligible cytotoxicity. Annexin V–FITC/PI imaging enabled visualization of the mode of cell death. No significant Annexin V or PI staining was detected for untreated, SNPs-treated, and ISNPs-treated cells under dark conditions. However, nearly the entire cell population exposed to ISNPs with NIR irradiation showed Annexin V and PI positivity and signs of morphological collapse (Fig. 3(e)) indicative of membrane damage and loss of viability due to photothermal injury.

Collectively, the data in Fig. 3 confirm that non-toxic ISNPs elicit robust and selective tumor cell damage upon NIR irradiation, and outside of the manipulable photothermal conversion, the membrane-disruptive feature of the ISNP can facilitate the expeditious release of DAMPs and promote subsequent downstream immune activation. The fact that ISNPs give rise to a polyphenol-mediated protein corona proposes the possibility of antigen-capturing carriers, which can engender antigen retention and presentation to amplify immune responses. The features, such as membrane permeabilization, ICD initiation and antigen capture, provide the mechanistic basis for the immunotherapeutic functionalities that ISNPs will exhibit in the requisite forthcoming *in vivo* studies.

2.4 ISNPs-induced membrane remodeling and immunogenic signaling

To examine whether these membrane effects were correlated with immunogenic damage-associated molecular patterns, CRT and HMGB1 subcellular distributions were assessed in PBS control, ISNPs, or ISNPs followed by 808 nm irradiation groups (Figs. 4(a) and 4(b)). The membrane and cortical actin were outlined with rhodamine–phalloidin, and nuclei were counterstained with Hoechst. With ISNPs alone, only modest CRT redistribution and limited HMGB1 perturbation were observed, suggesting that the saponin–polyphenol nanostructure may induce membrane-associated stress under the current conditions. In contrast, ISNPs followed by 808 nm irradiation resulted in pronounced CRT surface exposure and a substantial depletion of nuclear HMGB1, accompanied by diffuse redistribution. These observations are consistent with the well-established ICD-associated DAMP signatures reported for photothermal therapy (Figs. 4(a) and 4(b)) [38, 39].

To further examine whether antigen-associated ISNP treatment can promote dendritic-cell activation, bone marrow-derived dendritic cells (BMDCs) were incubated with Control, Antigen, ISNPs, or ISNPs+NIR@Antigen and analyzed by flow cytometry. Representative plots for CD86 and CD80 expression on $CD11c^+$ BMDCs are shown in Figs. 4(c) and 4(e), respectively, with the corresponding mean fluorescence intensity (MFI) quantification summarized in Figs. 4(d) and 4(f). In parallel, pro-inflammatory cytokines released into the culture supernatant (tumor necrosis factor-alpha (TNF-α), interleukin-1 beta (IL-1β), and interleukin-6 (IL-6)) were quantified by enzyme-linked immunosorbent assay (ELISA) (Fig. 4(g)), further supporting enhanced immune activation under our current conditions.

Collectively, these results indicate that saponin-mediated membrane perturbation may contribute to the priming of immunogenic stress signals, while NIR-induced photothermal activation serves as the dominant driver for the redistribution of DAMPs and downstream BMDC activation in this system [40].

2.5 Transcriptomic responses of 4T1 cells to ISNPs-mediated photothermal treatment

To characterize global molecular changes associated with ISNPs-mediated membrane remodeling and photothermal injury, bulk RNA sequencing was performed on the 4T1 cells treated with ISNPs plus 808 nm irradiation and the appropriate controls (Fig. 5). The heatmap of the top differentially expressed genes shows very coherent expression profiling per condition, reflecting excellent internal consistency of biological replicates (Fig. 5(a)). The principal-component analysis shows clear separation of the groups (Fig. 5(b)), and the sample-to-sample distance matrix (Fig. 5(d)) confirms high within-group similarity and low between-group similarity, highlighting the transcriptional response to ISNPs+NIR.

Differential-expression analysis revealed 240 differentially expressed genes: 110 upregulated and 130 downregulated transcripts (Fig. 5(c)). Representative of the upregulated genes were the classical markers of stress-response and damage-adaptation pathways, *Ddit3*, *Gadd45a*, and *Gdf15*. Their co-upregulation, together with the largely structured appearance of the group of differentially expressed genes in the heatmap (Fig. 5(a)), suggested that the transcriptional change is a regulated process and not an excessive nonspecific transcriptional collapse.

Gene Ontology (GO) analysis indicated that the up-regulated genes were strongly enriched for ion-channel activities and associations with sulfur compounds (Fig. 5(e)), highlighting engagement of host ion homeostasis and redox signaling pathways that are commonly activated during heat or membrane stress. Similarly, enrichment of biological-process terms indicated regulation of angiogenesis and vasculature development, and multiple forms of negative regulation of phosphorylation-dependent signaling, as well as processes related to production of cytokines and phosphate/heparin metabolism (Fig. 5(f)). Together with other evidence, these annotations suggest that ISNPs+NIR treatment elicits a coordinately activated program coupling stress-response signaling to regulation of both vascular and inflammatory activity.

Gene-set enrichment analysis provided further mechanistic understanding; the gene set "protection from natural killer cell–mediated cytotoxicity" was significantly enriched (Fig. 5(g)), indicating that innate immune interaction pathways are tuned following ISNPs-induced photothermal stress, consistent with CRT exposure and HMGB1 release observed previously in Fig. 4. To further incorporate the gene-level changes, a protein–protein interaction network was generated (Fig. 5(h)). A central stress-response module consisting of DDIT3, PPP1R15A, GADD45A, and GDF15, suggested activation of the integrated stress-response axis. A second cluster centered on CXCL10 and interferon-inducible genes such as *Ifit1* and *Ifit3*, indicating strong CXC chemokine signaling and interferon engagement. A few additional

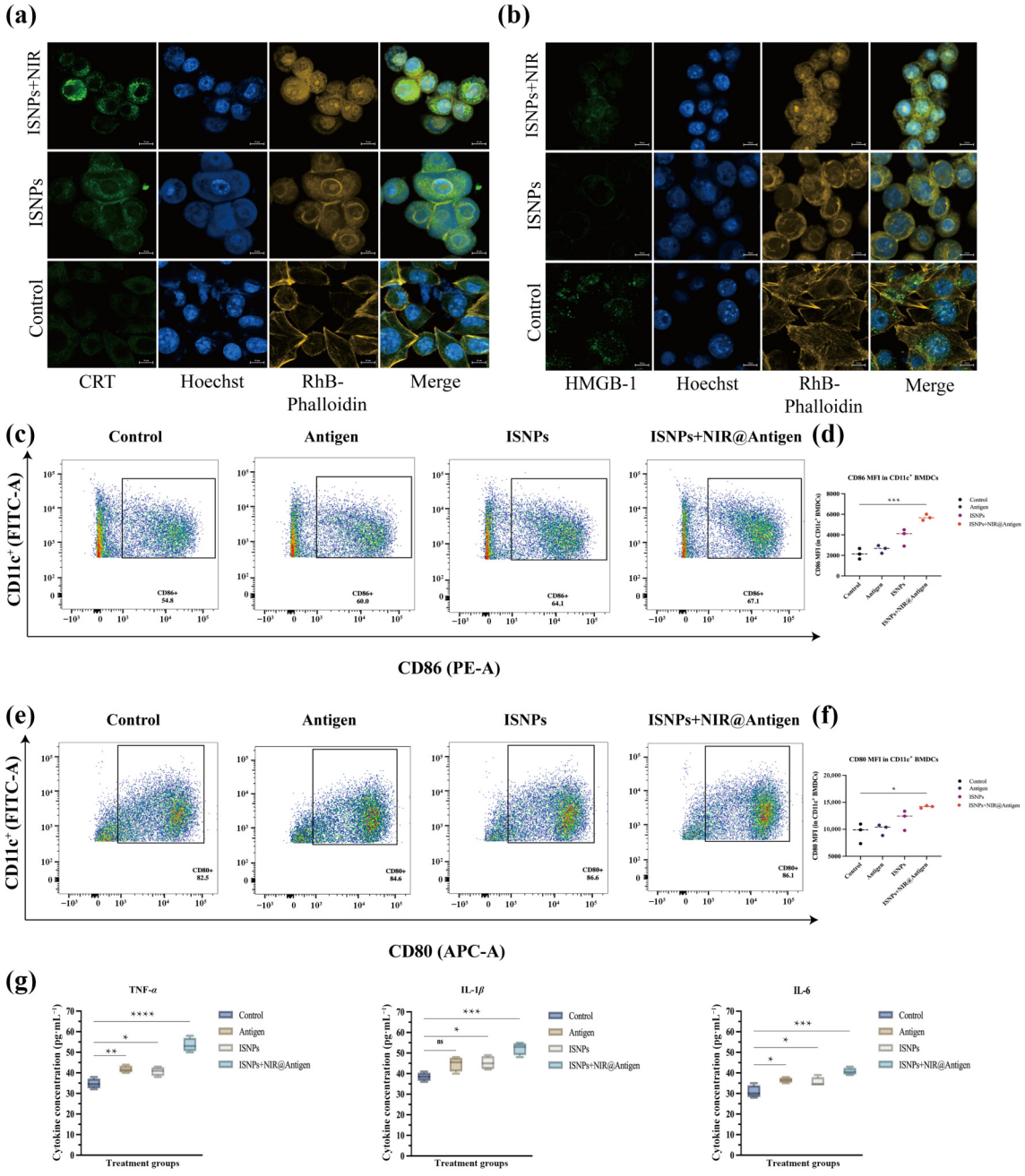

Figure 4 ISNPs-induced immunogenic signaling and dendritic-cell activation *in vitro*. Confocal images showing the subcellular distribution of (a) CRT and (b) HMGB1 in cells treated with PBS (Control), ISNPs, or ISNPs followed by 808 nm laser irradiation (ISNPs+NIR). CRT or HMGB1 was labelled with FITC (green); the plasma membrane and cortical actin were stained with rhodamine B–conjugated phalloidin (red); nuclei were counterstained with Hoechst 33342 (blue). The rightmost column shows merged channels. Scale bars: 10 μm. (c) Representative flow-cytometry plots of CD86 expression in $CD11c^+$ BMDCs following indicated treatments (Control, Antigen, ISNPs, and ISNPs+NIR@Antigen). (d) Quantification of CD86 MFI in $CD11c^+$ BMDCs. Each dot represents an independent replicate; technical outliers were excluded prior to analysis; final $n = 3$ per group. Data are shown as mean ± SD. Statistical analysis was performed using one-way ANOVA with Tukey's multiple-comparison test. (e) Representative flow-cytometry plots illustrating the expression of CD80 in $CD11c^+$ BMDCs following the indicated treatments. (f) Quantification of CD80 MFI in $CD11c^+$ BMDCs. Each dot represents an independent replicate; technical outliers were excluded prior to analysis; final $n = 3$ per group. Data are shown as mean ± SD. Statistical analysis was performed using one-way ANOVA with Tukey's multiple-comparison test. (g) ELISA quantification of TNF-α, IL-1β, and IL-6 in BMDC culture supernatants following indicated treatments. Data are expressed as mean ± SD ($n = 4$).

nodes, such as *Angptl6* and *Chka*, suggested additional changes in lipid and phosphate metabolism.

Collectively, the transcriptomic data demonstrate that ISNPs-mediated photothermal treatment elicits a highly ordered response featuring stress signaling, vascular–immune modulation, and metabolic reprogramming, divulging a molecular roadmap consistent with the plasma membrane remodeling, CRT exposure, and HMGB1 translocation in Fig. 4.

2.6 *In vivo* photothermal efficacy and immune-associated tumor remodeling

The *in vivo* therapeutic efficacy of ISNPs-mediated photothermal

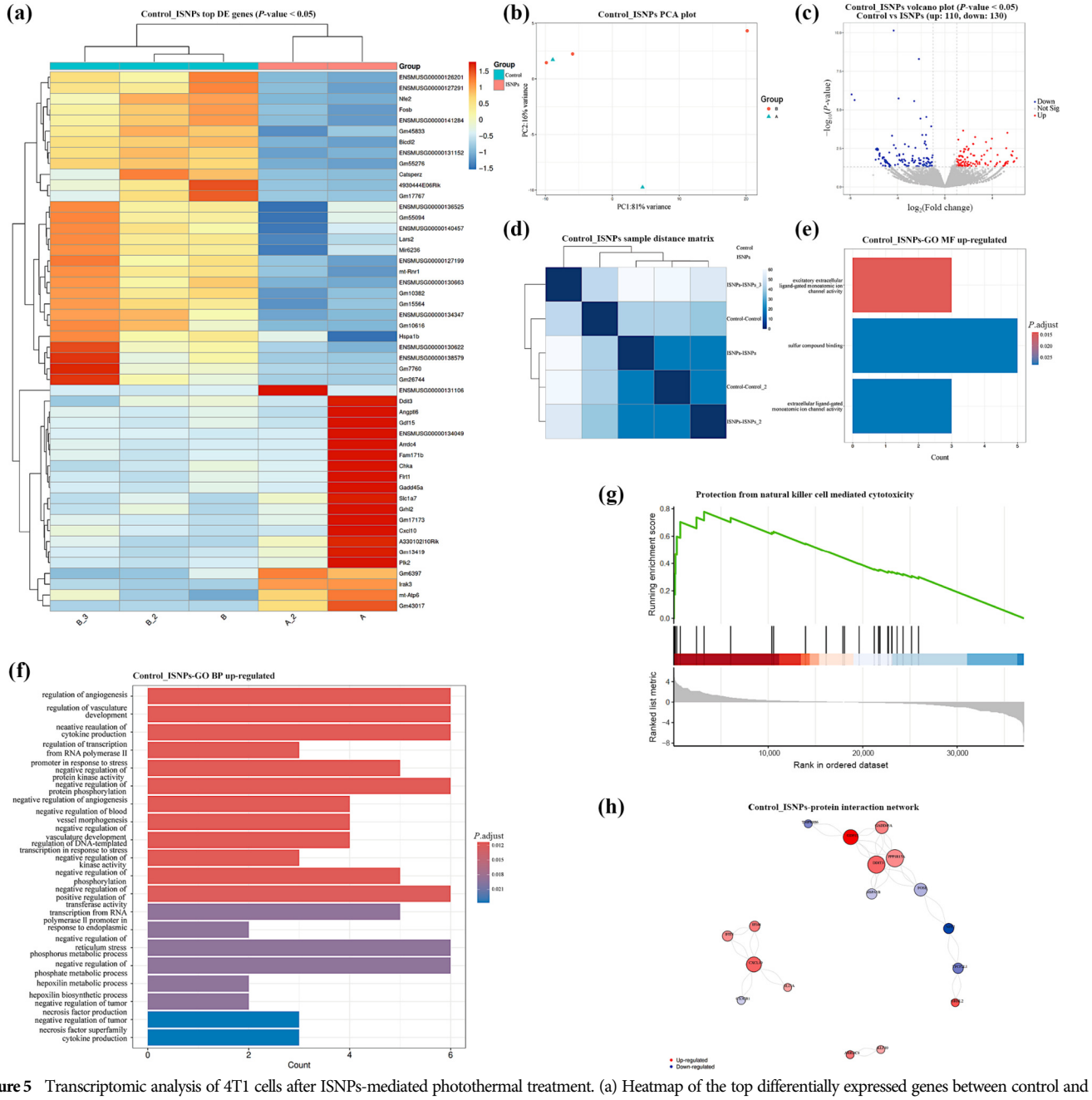

Figure 5 Transcriptomic analysis of 4T1 cells after ISNPs-mediated photothermal treatment. (a) Heatmap of the top differentially expressed genes between control and ISNPs+NIR-treated 4T1 cells. Columns represent individual samples and rows represent genes; colours indicate relative expression levels after row-wise scaling. (b) Principal-component analysis (PCA) plot of RNA-seq samples from control and ISNPs+NIR groups. Each point corresponds to one sample and is coloured according to treatment group. (c) Volcano plot of gene expression changes between ISNPs+NIR and control groups. The *x*-axis shows $\log_2$(Fold change) and the *y*-axis shows $-\log_{10}$(adjusted *P* value); significantly up- and down-regulated genes are marked according to predefined thresholds. (d) Sample-to-sample correlation heatmap with hierarchical clustering of control and ISNPs+NIR RNA-seq samples. Colours represent pairwise correlation coefficients between samples. (e) Gene Ontology (GO) enrichment of up-regulated genes in the molecular function (MF) category, displayed as a bar plot of selected MF terms. Bar length represents enrichment score or gene ratio. (f) GO enrichment of up-regulated genes in the Biological Process (BP) category, displayed as a bar plot of selected BP terms. Bar length represents enrichment score or gene ratio. (g) Gene-set enrichment analysis (GSEA) plot for the "protection from natural killer cell mediated cytotoxicity" pathway comparing ISNPs+NIR and control groups. The upper panel shows the enrichment score curve; the lower panel shows the ranked position of genes in this pathway. (h) Protein–protein interaction (PPI) network constructed from differentially expressed genes. Nodes represent proteins encoded by differentially expressed genes and are colored according to regulation status; edges represent predicted or known interactions.

treatment was assessed in a unilateral subcutaneous 4T1 tumor BALB/c mouse model as per the drug administration schedule depicted in Fig. 6(a). The body weights of each group of mice remained stable during the entire experiment (Fig. 6(b)), suggesting that the nanoparticle injection and the NIR irradiation were well tolerated with acceptable systemic tolerance. Tumor growth analysis revealed that mice treated with Control or ISNPs (without irradiation) exhibited tumor progression with limited suppression (Fig. 6(c)). Notably, ISNPs without irradiation produced only modest tumor growth delay, consistent with the design that

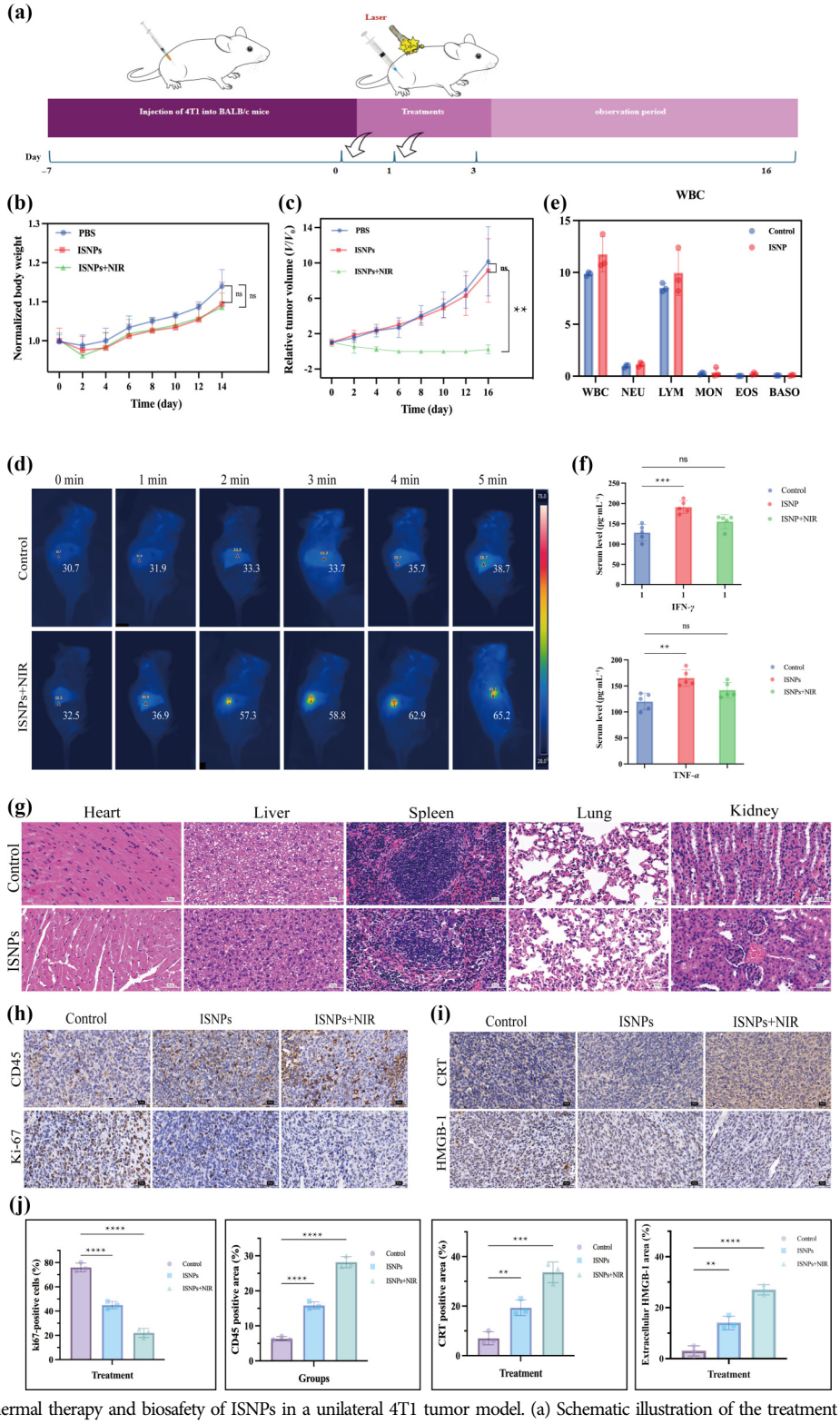

Figure 6 *In vivo* photothermal therapy and biosafety of ISNPs in a unilateral 4T1 tumor model. (a) Schematic illustration of the treatment protocol in BALB/c mice bearing subcutaneous 4T1 tumors, including tumor inoculation, intratumoral injection (saline or ISNPs), 808 nm laser irradiation, and follow-up. (b) Normalized body weight during treatment from day 0 to 14 (recorded every 2 days). (c) Tumor growth curves of 4T1 xenografts in mice treated with Control, ISNPs, and ISNPs+NIR. (d) Representative infrared thermal images of tumor sites in mice injected with saline (upper row) or ISNPs (lower row) under 808 nm irradiation at the indicated time points. (e) Representative hematological parameters post-treatment, including WBC, NEU, LYM, MON, EOS, and BASO counts (remaining indices shown in Fig. S2 in the ESM). (f) Serum levels of IFN-γ and TNF-α quantified by ELISA assays, indicating systemic immune responses elicited by different treatments. Data are mean ± SD (n = 3). Statistical analysis was performed using one-way ANOVA with Tukey's multiple-comparison test. (g) H&E staining of major organs (heart, liver, spleen, lung, and kidney) collected at the end of treatment from each group (scale bars: 50 μm). (h) Immunohistochemical staining of Ki-67 and CD45 in tumor sections from the different treatment groups (scale bars: 50 μm). (i) Immunohistochemical staining of CRT and HMGB1 in tumor sections from the different treatment groups (scale bars: 50 μm). (j) Quantification of Ki-67, CD45, CRT, and extracellular HMGB1 staining.

photothermal activation is required to elicit robust cytotoxicity and ICD cues *in vivo*. In comparison, ISNPs combined with 808 nm irradiation resulted in a strong and durable blockade effect on tumor growth to keep tumor volumes close to baseline for over ten days, after which only a slight resumption of growth was observed. This confirms that ISNPs-mediated photothermal activation provides *in vivo* tumor cytotoxicity. Infrared thermal imaging confirmed efficient photothermal conversion *in situ*. Tumors treated with ISNPs quickly warmed to ~ 58–65 °C upon irradiation, while tumors treated with Control were only ~ 32–38 °C under the same conditions (Fig. 6(d)). Such temperatures are in the vicinity of those which cause irreversible thermal injury, in line with the membrane rupture/immunogenic injury observed *in vitro*.

Systemic biosafety was evaluated by routine hematology. Routine hematology parameters (Fig. 6(e)) fell within normal physiological ranges. Full hematology panels of three representative mice per group are provided in Fig. S2 in the ESM, further supporting the absence of hematological toxicity. Additionally, serum levels of proinflammatory cytokines interferon-gamma (IFN-γ) and TNF-α were measured by ELISA (Fig. 6(f)). ISNPs and ISNPs+NIR both elevated cytokine levels, indicating systemic immune activation. Interestingly, the ISNP group showed higher cytokine levels than ISNP+NIR, which may be due to rapid tumor ablation in the NIR group reducing antigen availability and dampening prolonged immune stimulation. Further necropsy photographs are presented in Fig. S5 in the ESM. Hematoxylin and eosin (H&E) staining of major organs (heart, liver, spleen, lung, and kidney) showed no obvious pathological abnormalities across groups (Fig. 6(g)). Ki-67 staining demonstrated abundant proliferating nuclei in control tumors, but the ISNPs+NIR group exhibited decreased Ki-67 positive nuclei (Fig. 6(h)). The Ki-67-positive fraction was further quantified in Fig. 6(j). In parallel, in CD45 immunostained sections, infiltration of leukocytes was significantly augmented in ISNPs+NIR-treated tumors (Fig. 6(h)). CD45-positive staining was quantified in Fig. 6(j).

To ascertain whether these intratumoral changes were accompanied by immunogenic-damage signals, tumors were stained for CRT and HMGB1. In the Control and ISNPs groups, CRT was observed intracellularly and HMGB1 was localized to tumor cell nuclei. By contrast, CRT surface exposure and HMGB1 depletion from nuclei with concomitant extracellular redistribution (Fig. 6(i)) were significantly enhanced in ISNPs+NIR tumors, suggesting features consistent with hallmarks of immunogenic cell death. These changes were quantitatively analyzed in Fig. 6(j). Collectively, these observations correlated well with the danger-signal release and membrane remodeling observed *in vitro*.

Overall, we show that ISNPs facilitate *in vivo* potent photothermal tumor suppression with systemic safety, while local ISNPs-activated heating remodels the tumor microenvironment through immune-cell infiltration and CRT exposure and HMGB1 release, indicating photothermally driven, immunogenic remodeling of the tumor microenvironment and prompting further evaluation of systemic antitumor immunity in a bilateral tumor model.

2.7 ISNPs photothermal ablation achieves robust local control with a modest abscopal trend in a bilateral 4T1 model

To confirm whether ISNPs-mediated photothermal therapy induces a systemic rather than simply localized antitumor effect (i.e., beyond local tumor ablation), bilateral 4T1 tumor models were established on both flanks with intratumoral therapy given only to the primary (left) tumor (Fig. 7(a)). In the saline and ISNPs groups, primary tumors constantly grew in comparison, and their growth curves exhibited trends that tended to overlap (Fig. 7(b)). In contrast, ISNPs and 808 nm combined irradiation produced quick and lasting suppression of tumors, with some animals nearing total regression of their underlying treated disease. From these data, we suggest that ISNPs-mediated photothermal heating produces lasting localized control of the primary tumor, though what occurred at the level of distant (unaffected) tumors represents the hallmark of a systemic effect; tumors appearing contralateral to the treated site in saline and ISNPs groups were progressively larger, whereas tumors in mice treated with ISNPs+NIR at their primary site exhibited only a modest trend toward delayed growth in the contralateral tumors, and the overall differences over time were not statistically significant under the current conditions (Fig. 7(c)). All groups started with $n = 5$; due to non-treatment-related mortality, curves reflect the remaining animals at each time point (details in figure legend). Notably, an endpoint comparison at day 12 indicated a modest reduction in distant tumor size for ISNPs+NIR versus control. Primary size and distant size were correlated positively across animals (Fig. 7(d)), suggesting that effective local ablation may be associated with a limited systemic impact in this model. Body weights across animals remained constant (Fig. 7(e)).

Histological responses complemented the local and systemic findings. H&E staining readily revealed live tumor cells and preserved architecture in the saline and ISNPs groups, but widespread necrosis, nuclear fragmentation and structural disintegration were evident in the primary tumors of mice subjected to ISNPs+NIR (Fig. 7(f), top). Interestingly, the distant tumors of ISNPs+NIR-treated mice also contained patches of cell damage and necrotic fragmentation that were either not present or much reduced in control groups (Fig. 7(f), bottom), consistent with a modest systemic effect rather than merely a growth delay.

Immunohistochemical analysis further indicated that $CD45^+$ leukocyte infiltration was enhanced in ISNPs+NIR-treated tumors, particularly at the primary site (Figs. 7(g)–7(i)). In parallel, CD11c staining was also increased after ISNPs+NIR, consistent with elevated antigen-presenting cell-associated signals in the tumor microenvironment (Figs. 7(g)–7(i)).

Collectively, these results demonstrate potent local control as a consequence of single-tumor ISNPs-mediated photothermal ablation, accompanied by a modest trend of abscopal suppression in contralateral lesions under the current conditions. The findings indicate that the coincident escalations in $CD45^+$ leukocyte infiltration and CD11c-associated signals, in conjunction with the favorable body-weight profile, lend support to a hypothesis in which acute photothermal injury is coupled to immune engagement while maintaining acceptable systemic tolerability.

3 Conclusions

ISNPs, formed through co-assembly of tannic acid and saponin, provide a bioactive, membrane-altering nanosystem capable of combined photothermal conversion and immunogenic activity. Instead of mediating cellular toxicity purely by a heat-mediated mechanism, ISNPs present potent membrane-altering bioactivity inducing rapid release and expulsion of DAMPs (CRT and HMGB1) and promoting nuclear envelope destabilization of cells

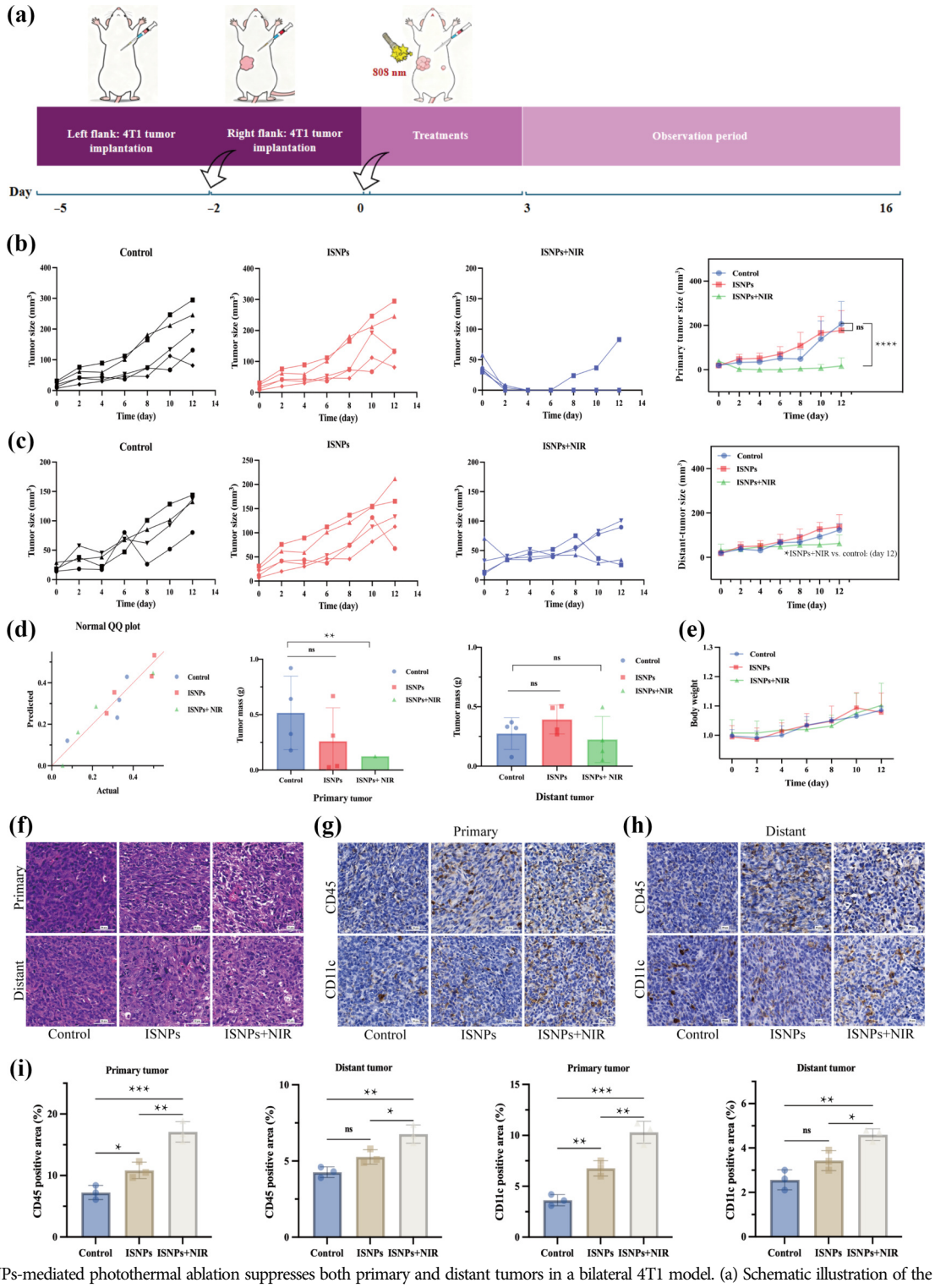

Figure 7 ISNPs-mediated photothermal ablation suppresses both primary and distant tumors in a bilateral 4T1 model. (a) Schematic illustration of the bilateral tumor model and treatment workflow. ISNPs or PBS (Control) were injected intratumorally into the primary (left) tumor, followed by 808 nm irradiation where indicated; the distant (right) tumor received no treatment. (b) Primary tumor growth curves for Control, ISNPs, and ISNPs+NIR groups, started with $n = 5$; n decreased due to non-treatment-related mortality (Control and ISNPs+NIR: $n = 4$ after the 4th measurement). ISNPs+NIR resulted in pronounced suppression of primary tumor progression. Means and error bars were calculated using the available animals at each time point. (c) Individual growth curves of distant tumors (each line represents one mouse). Statistical analysis was performed using two-way ANOVA (treatment × time) with multiple comparisons. Data are shown as mean ± SD. No statistically significant differences were observed among groups for distant tumor growth over time. An endpoint comparison at day 12 showed a modest reduction in distant tumor size in the ISNPs+NIR group versus the control group ($^*P < 0.05$). (d) Correlation between final primary-tumor and distant-tumor volumes, showing that stronger ablation of the primary site is associated with reduced outgrowth of distant lesions. (e) Body-weight changes during treatment, showing no significant weight loss. (f) H&E staining of primary (top) and distant (bottom) tumors (scale bars: 50 μm). Immunohistochemical staining of CD45 and CD11c in (g) primary and (h) distant tumors. Scale bars: 50 μm. (i) Quantification of CD45$^+$ and CD11c$^+$ staining shown as positive area fraction (%). Statistical analysis was performed using one-way ANOVA with Tukey's multiple-comparison test; significance is denoted as ns (not significant), $^*P < 0.05$, $^{**}P < 0.01$, $^{***}P < 0.001$, $^{****}P < 0.0001$.

enhancing innate immunogenic signals. The polyphenolic interface provides the system with antigen-binding capability allowing *in situ* retention of tumor-associated proteins and promoting their uptake by dendritic cells through plasma membrane perturbation and antigen capture. This results in the activation of two key processes: the induction of cell death, and an immunological response within the microenvironment of the tumor.

4 Experimental

4.1 Reagents

Analytical-grade TA and SAP (≥ 60%) were obtained from Aladdin Biochemical Technology Co., Ltd. in Shanghai, China. Doxorubicin hydrochloride (DOX, ≥ 98%) and ICG were obtained from Macklin Biochemical Technology Co., Ltd. in Shanghai, China. Hoechst 33342, Calcein-AM/PI Live/Dead Kit, mouse, IgG-FITC, 3,3'-dioctadecyloxacarbocyanine perchlorate (Dio), anti-HMGB1, anti-CRT polyclonal antibodies, BCA Protein Assay Kit, and Annexin V-FITC/PI Apoptosis Detection Kit were purchased from Solarbio Life Sciences (Beijing, China). Cell Counting Kit-8 (CCK-8) and LDH Assay Kit were obtained from Beyotime Biotechnology (Shanghai, China). Dulbecco's modified Eagle medium (DMEM), phosphate buffered saline (PBS), and Penicillin-Streptomycin (PS) were obtained from Gibco (USA). Fetal bovine serum was purchased from Umedium (3023A, Hefei, China) and Ultrapure Deionized Water (18.2 MΩ·cm) was obtained from a Milli-Q purification system.

4.2 Equipments

Nanoparticle morphology (SNPs/ISNPs) was examined by transmission electron microscopy (TEM, HT7800, Hitachi, Japan). Live-cell fluorescence imaging (Calcein-AM/PI staining, DCFH-DA–based ROS detection, and Annexin V-FITC/PI apoptosis analysis) was performed on confocal laser scanning microscopy (CLSM, FV3000RS, Olympus, Japan).

4.3 Cells and animals

Breast cancer cells from mice were obtained from American Type Culture Collection (ATCC). Culture medium included 10% fetal bovine serum and Dulbecco's Modified Eagle Medium (DMEM). Cells were routinely maintained in monolayer culture at 37 °C in 5% CO_2. BALB/c mice (Female, 6–8 weeks, Beijing Vital River Laboratory Animal Technology Co., Ltd., Beijing, China) were maintained under specific-pathogen-free (SPF) condition with free access to food and water. Male C57BL/6 mice used as BMDC donors are described in Section 4.15. All animal procedures were approved by the Laboratory Animal Center of Tsinghua University (Approval No. 24-ZLY1).

4.4 Synthesis of SNPs and ICG-loaded ISNPs

Stock solutions of TA (50 mg·mL^{-1}) and SAP (50 mg·mL^{-1}) were prepared in deionized water, and ICG stock solution was prepared at 1 mg·mL^{-1}. For ISNP preparation, TA, SAP and ICG solutions were mixed and allowed to stand at room temperature overnight to enable co-assembly. Unless otherwise specified, 400 μL of each component solution (TA, SAP and ICG) was used per batch. Under this standard condition, the nominal feed masses were 20 mg TA, 20 mg SAP and 0.4 mg ICG. Nanoparticles were collected by centrifugation (10,000 rpm, 10 min), washed with deionized water, and re-dispersed by brief sonication to minimize residual aggregation. The collected nanoparticles were dried at 60 °C in an oven to constant weight, and the overall yield was ~ 56.8% based on dried mass. The collected SNPs were dried at 60 °C to constant weight; yields were comparable to those of ISNPs. Unless otherwise stated, nanoparticle concentrations reported in this work refer to the mass concentration of dried nanoparticles (mg·mL^{-1}) after collection and drying, rather than the mass of any individual constituent.

4.5 CCK-8 cytotoxicity and *in vitro* photothermal therapy

4T1 cells were plated in 96-well plates at 5 × 10^3 cells/well and allowed to adhere and incubate for 24 h at 37 °C, 5% CO_2. For dose–response cytotoxicity, cell culture medium was replaced by DMEM–SNPs or DMEM–ISNP suspensions containing SNPs or ISNPs at concentrations of 0, 0.01, 0.02, 0.09, 0.19, 0.38, 0.75, or 1.50 mg·mL^{-1} and incubated for a further 24 h. Supernatants were carefully decanted and wells rinsed three times with PBS. A mixture of 10 μL of CCK-8 and 90 μL of serum-free DMEM per well was added for 45 min at 37 °C; absorbance was read at 450 nm. Blanks of reagents and controls of medium alone were used for background subtraction. For PTT, the culture medium was replaced with ISNPs-dosed DMEM (100 μg·mL^{-1}), and the cells were irradiated with the laser at 808 nm at 0, 1.0, 1.5, or 2.0 W·cm^{-2} for 3 min before being returned to the incubator for 24 h. Cell viability was measured by the same CCK-8 procedure, with the ISNPs/no-irradiation (0 W·cm^{-2}) group serving as the PTT control. All cultures in all conditions were accomplished in triplicate wells and repeated thrice in independent experiments.

4.6 UV–Vis absorption spectroscopy

The UV–Vis absorption spectra of the various ICG, TA, SAP, SNPs physical mixture, and ISNP formulations were acquired on a fluorescence spectrophotometer with UV detection across the 400–900 nm wavelength range. Each sample was prepared as a dispersion in deionized water at an ICG concentration of 5 μg·mL^{-1}. Samples were loaded into 96-well plates for acquisition. Spectra were normalized to compare optical profiles across all formulations. Each sample was taken in triplicate.

4.7 FTIR spectroscopy

FTIR spectroscopy was performed to investigate the chemical interactions between ICG and SNPs, and their resultant composite (ISNPs). The samples were lyophilized to a powder and mixed with anhydrous KBr at a ratio of between ~ 1:100 (w/w), then finely ground and pressed into pellets. Infrared spectra were recorded on an FTIR spectrometer (Thermo Fisher Scientific, USA) in the range from 4000 to 500 cm^{-1}, at a resolution of 4 cm^{-1}, with 25 scans averaged per sample, and were compared to analyze any potential intermolecular interactions.

4.8 ICG encapsulation in ISNPs

ISNPs were prepared as self-assembled aggregates composed of saponin and TA in water, into which ICG was infused at a variety of concentrations. In essence, saponin and TA (50 mg·mL^{-1} each) were mixed at varied volumes with ICG stock solutions before infusion to final concentrations of 0.0833 to 0.43 mg·mL^{-1} and were allowed to self-assemble in solution at room-temperature for 30 min whilst gently stirring. The assembled nanoparticle suspension was centrifuged at 10,000 rpm for 10 min to eliminate free ICG.

The supernatant was separated and the amount of unencapsulated ICG was calculated by reference to a standard calibration curve based on the UV–Vis absorbance at 780 nm. The drug loading (DL%) and encapsulation efficiency (EE%) of ICG were determined using the following equations (Eqs. (1) and (2)):

$$\text{DL}\ (\%) = \frac{\text{Mass of encapsulated ICG}}{\text{Mass of ISNPs}} \times 100 \quad (1)$$

$$\text{EE}\ (\%) = \frac{\text{Mass of encapsulated ICG}}{\text{Mass of ICG initially added}} \times 100 \quad (2)$$

4.9 Real-time imaging of immediate morphological responses

4T1 cells were plated in 6-well plates at a density of 5×10^5 cells/well and allowed to adhere overnight. Media was then exchanged for fresh DMEM containing either SAP (5 mg·mL^{-1}) or SNPs (2 mg·mL^{-1}); controls were presented with fresh DMEM only. Immediately post-dosing and continuing for 30 min, frames of cells were monitored on an inverted bright-field microscope, and frames were saved every 30, 60 and 90 s to record rapid morpho dynamic events (rounding, membrane blebbing, detachment), $n = 3$ independent wells per condition.

4.10 LDH release (membrane integrity) assay

Cytotoxicity and damage to membranes after ISNPs exposure were assessed with a commercial LDH kit (Solarbio, M1030, Beijing, China) following the manufacturer's instructions with the parameters defined here for reproducibility. 4T1 cells were seeded into 96-well plates at a density of 1×10^4 cells/well and allowed to adhere overnight as above. Cells were then treated with ISNPs (100 or 200 μg·mL^{-1}) under dark conditions. For the photothermal condition, cells treated with ISNPs (200 μg·mL^{-1}) were additionally irradiated with an 808 nm laser using the same parameters as described in the main text. After treatment, culture supernatants were segregated for determination of extracellular LDH. Absorbance was measured at 490 nm. All conditions were assessed with $n = 4$ independent replicates, and data are presented as mean ± standard deviation (SD).

4.11 *In vitro* photothermal performance

ISNPs and SNPs dispersions were dispersed in deionized water. Photothermal heating under 808 nm continuous wave irradiation was acquired thermograms with FOTRIC 225 thermal imager at 1 min intervals. Benchmarking using ISNPs, blank SNPs and deionized water all irradiated under the same conditions (1.0 W·cm^{-2} exposure, 5 min) were performed.

Power dependence was obtained for constant concentration of ISNPs. To evaluate the power dependence, an ISNP dispersion (200 μg·mL^{-1}) was irradiated at 0.5, 1.0, 1.5, and 2.0 W·cm^{-2} for 5 min. Then the concentration dependence at 1.0 W·cm^{-2} was obtained with ISNPs dispersions of 50, 100, 200, 400, and 800 μg·mL^{-1} (5 min). For photothermal stability, five on/off cycles in a row (1.0 W·cm^{-2} exposure time 3 min) continuous thermal recording were performed. All experiments were performed in triplicate.

4.12 Cell viability and apoptosis analysis

For *in vitro* imaging studies, 4T1 cells were seeded in a 4-well confocal dish at 1×10^5 cells/well for 24 h to attach. The media was replaced with DMEM containing ISNPs (0, 50, 100, 200 μg·mL^{-1}) for 1 h, and cells were irradiated with an 808 nm laser at 0, 1.0, 1.5, or 2.0 W·cm^{-2} for 3 min, then incubated for 6 h. The media was replaced, cells were washed with cold PBS twice and then stained with Calcein-AM and PI (15 min, dark) before collecting fluorescence images on confocal laser scanning microscope.

The DOX fluorescence experiment began when the ISNPs medium in which cells were maintained was removed and replaced with DMEM plus DOX at the appropriate concentration for the experiment. Cells that had undergone laser treatment were then imaged with a fluorescence camera set to detect red Dox fluorescence.

4.13 Cellular uptake assay

4T1 cells were seeded into confocal culture dishes at a density of 1×10^5 cells per well and left to adhere for 24 h. The next day the old medium was discarded and replaced by DMEM containing free ICG or ISNPs (ICG conc. 5 μg·mL^{-1}) and the cells were co-incubated with the preparations for 1 h at 37 °C. After co-incubation, the medium was removed and each well washed three times with PBS. The samples were fixed using 4% paraformaldehyde for 15 min and followed by Hoechst 33342 (5 μg·mL^{-1}) for nuclei labelling for a further 15 min. Immediately following the PBS wash, the fluorescence imaging was performed via confocal laser scanning microscopy. The fluorescent signal from ICG was detected in the red channel, while Hoechst-stained nuclei were detected in the blue channel.

4.14 Immunogenicity-related protein and membrane staining assay

4T1 cells were seeded at 1×10^5 cells per well in confocal dishes and incubated for 24 h; then the cells were divided into three groups: a control group receiving fresh DMEM, an ISNPs group treated with ISNPs (ICG-equivalent concentration), and an ISNPs+NIR group in which they were treated with ISNPs in the same way as above and then irradiated with 808 nm NIR light at 1.5 W·cm^{-2} for 3 min. The groups were incubated for a further 1 h. The cells were washed thrice with PBS and fixed in 4% paraformaldehyde for 15 min and then permeabilized with 0.1% Triton X-100 for 10 min. Blocking was done with 0.5% BSA for 1 h at room temperature.

Primary antibodies against CRT or HMGB1 were added and incubated overnight at 4 °C. After washing with PBS, samples were treated with green-fluorescent (anti-species) goat anti-rabbit IgG secondary antibodies from Life Technologies for 1 h in the dark. For membrane structures, samples were labelled with rhodamine B-conjugated phalloidin for 30 min. Nuclei were counterstained with Hoechst 33342 for 15 min then washed again with PBS and imaged on a confocal laser scanning microscope. Green represents secondary-antibody-labelled CRT or HMGB1, rhodamine B is seen in the membrane, and Hoechst stains nuclei.

4.15 BMDC preparation, flow cytometry for maturation markers, and cytokine ELISA

BMDCs were generated from male C57BL/6 mice (7 weeks old; Beijing Vital River Laboratory Animal Technology Co., Ltd., Beijing, China). The femurs and tibias were harvested under sterile conditions, and bone marrow was extracted using RPMI-1640. Following centrifugation at 500*g* for 5 min, red blood cells were

lysed using RBC lysis buffer (1 mL per mouse, 1 min). This was followed by quenching with RPMI-1640 and centrifugation at 500*g* for a further 5 min. The cells were then resuspended in complete RPMI-1640 (10% FBS, 1% Penicillin–Streptomycin) supplemented with recombinant murine GM-CSF (10 ng·mL^{-1}) and IL-4 (50 ng·mL^{-1}). The cells were seeded into 24-well plates (1 mL per well) and cultured at 37 °C with 5% CO_2. On the second day, non-adherent cells were meticulously removed, and fresh cytokine-containing medium was added. Half-medium exchange was performed on days 5 and 7 using the same cytokine-supplemented medium. On the seventh day, loosely adherent/suspended cells were collected as BMDCs for subsequent assays. C57BL/6 mice were used as BMDC donors due to availability and robust BMDC yield in our facility.

BMDCs were subjected to treatment with Control, Antigen, ISNPs, or ISNPs+NIR@Antigen (20 μg·mL^{-1}) for a duration of 24 h. For NIR activation, samples were irradiated under the same 808 nm parameters that had been previously described. BMDCs were collected without trypsinization, washed with FACS buffer (PBS containing 0.5% BSA), and stained with fluorophore-conjugated antibodies against CD11c (FITC), CD86 (PE), and CD80 (APC) for 30 min at 4 °C in the dark. The cells were washed once and acquired on a BD FACSAria II cytometer. The subsequent analysis of the data involved the gating of singlets and CD11c$^+$ BMDCs, followed by the quantification of CD80 and CD86 expression (MFI).

Culture supernatants were collected after 24 h stimulation, clarified by centrifugation (500*g*, 5 min), and analyzed using Solarbio ELISA kits for TNF-α, IL-6, and IL-1β (Solarbio, China; cat. no. 1217202, 1210122, and 1210602, respectively) according to the manufacturers' instructions.

For flow-cytometry analysis, predefined QC criteria (e.g., abnormal event counts, unstable signal, or aberrant CD11c$^+$ gating) were applied to identify technical outliers prior to statistical analysis. Samples failing QC were excluded, and the remaining samples were used for MFI quantification (final n = 3 per group). Within-group variability was evaluated using the coefficient of variation (CV).

4.16 RNA sequencing and sample preparation

4T1 cells were seeded in 6-well plates (cell culture) and cultured for 24 h, then placed in three groups (Control, ISNPs, ISNPs+NIR). Cells in the ISNPs and ISNPs+NIR groups were treated with ISNPs for 24 h. The ISNPs+NIR group was then irradiated with an 808 nm laser at a fluence of 1.0 W·cm^{-2} until the temperature reached ~ 48 °C and then the culture was irradiated for 1 min. The Control and ISNPs were not irradiated.

Cells were trypsinized, harvested, and washed twice with cold PBS. Cells were pelleted and resuspended in RNA-protect Cell Reagent (Qiagen) and stored at −80 °C until RNA extraction. Total RNA was extracted using TRIzol reagent. Qualified RNA samples were delivered to a laboratory certified by a 3rd entity for transcriptome analysis. DEGs were defined using $|\log_2 FC| \geq 1$ and $P < 0.05$.

4.17 *In vivo* anti-tumor therapy

For the 4T1 tumor model, 1 × 10^6 4T1 cells (PBS suspension) were injected subcutaneously into the right flank of BALB/c mice. When the tumors reached 80–100 mm^3 in size, mice were divided randomly into three groups (n = 5) named Control, ISNPs, and ISNPs+NIR. 100 μL of either PBS (Control) or ISNPs (suspended in PBS, 1 mg·mL^{-1}) were injected intratumorally per mouse. Five minutes after injection, the tumor on the mouse in the ISNPs+NIR group was irradiated by 808 nm laser (1.5 W·cm^{-2}) for 5 min. Thermal images were acquired using FOTRIC infrared camera at 0, 1, 2, 3, 4, and 5 min intervals in order to assess tumor local temperature elevation. Control and ISNPs groups were not irradiated. Tumor size and the weight of the body were recorded every other day beginning on day 0 and measured across seven time points. Tumor volume was calculated using Eq. (3):

$$V = \frac{\text{Length} \times \text{Width}^2}{2} \tag{3}$$

At the endpoint of the study, the mice were sacrificed. Major organs (heart, liver, spleen, lung, kidney) from all groups were collected for the purpose of H&E staining to assess toxicity. Tumors were collected and subject to Ki67, CRT, HMGB1 and CD45 immunohistochemistry to assess therapeutic response and immunogenic cell death. CD45-positive staining was quantified by ImageJ using color deconvolution (DAB) and reported as positive area fraction with identical thresholds. For systemic biosafety evaluation, non-tumor-bearing BALB/c mice were divided into Control and ISNPs groups (n = 3), with each mouse receiving an intratumoral injection of 100 μL PBS (set as Control) or 100 μL ISNPs (1 mg·mL^{-1}). Whole blood was sampled from these mice after 24 h for hematological evaluations.

4.18 Bilateral tumor model

To evaluate systemic antitumor immune responses induced by local treatment, a bilateral 4T1 mammary tumor model was established in female BALB/c mice (6–8 weeks old). Subsequently, on day −5, a subcutaneous injection of 100 μL PBS containing 1 × 10^6 4T1 cells was administered to each mouse into the left flank, thereby establishing the primary tumor. To simulate distant metastatic lesions, 1 × 10^6 4T1 cells were reinjected into the right abdomen on day −2, thereby establishing a bilateral tumor model. At the point at which the primary tumor volume reached 80–100 mm^3 (day 0), the mice were randomly divided into three groups (n = 5 per group). The present study focuses on the use of PBS control, laser-free ISNPs, and NIR-irradiated ISNPs.

For treatment, 100 μL of PBS or an ISNPs suspension was injected into the primary tumor via the intratumoral. The ISNPs+NIR group received immediate near-infrared irradiation with an 808 nm laser at a power density of 1.0 W·cm^{-2} for a duration of 5 min, with the laser targeting exclusively the primary tumor site. The ISNPs group received only the nanoparticle formulation injection, without subsequent irradiation. In the experimental design, all groups were subjected to untreated contralateral (right-side) tumors, with the objective of assessing the effects of these tumors on a distant site.

Bilateral tumor growth was monitored at 2-day intervals using electronic calipers, with volume calculated according to standard formulae. The volume of the subject is calculated as follows (Eq. (4)):

$$V = \frac{\text{Length} \times \text{Width}^2}{2} \tag{4}$$

The body weight of the subject was concurrently recorded to assess systemic toxicity. On day 14, the mice were euthanized, and the tumors were excised, weighed, and documented. The tumor tissue was then subjected to further processing for the purpose of

conducting histological and immunological analyses. All animal experiments were conducted in accordance with the established ethical guidelines and received approval from the Institutional Animal Care and Use Committee.

4.19 Statistics and reproducibility

Data are presented as mean ± SD as indicated in figure legends. Statistical analyses were performed using GraphPad Prism. For comparisons among multiple groups, one-way ANOVA followed by Tukey's multiple-comparison test was used. For tumor growth curves over time, two-way ANOVA with appropriate multiple-comparison correction was applied. Significance is denoted as ns ($P > 0.05$), *$P < 0.05$, **$P < 0.01$, ***$P < 0.001$, and ****$P < 0.0001$.

Electronic Supplementary Material: Supplementary material (supplementary material includes additional cell viability assays, membrane disruption analysis, splenocyte cytotoxicity evaluation, representative tumor photographs, and hematological analysis related to the biosafety assessment of ISNPs) is available in the online version of this article at https://doi.org/10.26599/NR.2026.94908614.

Data availability

All data generated and analyzed during this study are available in the paper and its Supplementary Information files and from the corresponding author on request. Source data are available in this paper.

Acknowledgements

This work was financially supported by the grants of the National Natural Science Foundation of China (Nos. 32501239, 51971116, and 81671829). We thank D. J. T. for intellectual inspirations.

Declaration of competing interest

There are no conflicts to declare.

Author contribution statement

B. L. M., J. S. L., and H. A. performed the experiments and analyzed the results. L. Y. Z., Y. W., J. Y., and S. L. C. provided critical suggestions for this work. B. L. M. wrote the original manuscript. J. S. L., Y. W., and L.Y. Z. supervised the project and reviewed the manuscript.

Informed consent

Not applicable.

Ethics statement

All animal experiments were approved by the Laboratory Animal Center of Tsinghua University (Approval No. 24-ZLY1) and performed in accordance with institutional guidelines for animal care and use.

Use of AI statement

None.

References

[1] Azrial, F. Potential of bioactive compounds in Indonesian endemic nutmeg (*Myristica fragrans* and *Myristica argentea*) and their applications in health: An overview. *J. Evidence-based Nurs. Public Health* **2025**, *2*, 121–137.

[2] Dhas, N.; García, M. C.; Kudarha, R.; Pandey, A.; Nikam, A. N.; Gopalan, D.; Fernandes, G.; Soman, S.; Kulkarni, S.; Seetharam, R. N. et al. Advancements in cell membrane camouflaged nanoparticles: A bioinspired platform for cancer therapy. *J. Controlled Release* **2022**, *346*, 71–97.

[3] Zhu, D. M.; Tuo, W. B. QS-21: A potent vaccine adjuvant. *Nat. Prod. Chem. Res.* **2016**, *3*, e113.

[4] den Brok, M. H.; Nierkens, S.; Wagenaars, J. A.; Ruers, T. J.; Schrier, C. C.; Rijke, E. O.; Adema, G. J. Saponin-based adjuvants create a highly effective anti-tumor vaccine when combined with *in situ* tumor destruction. *Vaccine* **2012**, *30*, 737–744.

[5] Yu, L. N.; Jin, Y.; Song, M. J.; Zhao, Y.; Zhang, H. Q. When natural compounds meet nanotechnology: Nature-inspired nanomedicines for cancer immunotherapy. *Pharmaceutics* **2022**, *14*, 1589.

[6] Khan, A. A.; Allemailem, K. S.; Almatroudi, A.; Almatroodi, S. A.; Mahzari, A.; Alsahli, M. A.; Rahmani, A. H. Endoplasmic reticulum stress provocation by different nanoparticles: An innovative approach to manage the cancer and other common diseases. *Molecules* **2020**, *25*, 5336.

[7] Lu, J. S.; Ma, B. L.; Li, Y.; Chen, S. M.; Zhang, M. Y.; Guo, Z. H.; Gao, X. H.; Neema, U. P.; Fahad, A.; Xie, W. S. et al. *Saponin*-mediated cell membrane interference nanomedicine potentiates tumor chemo-immunotherapy via a perforin-granzyme-like mechanism. *Biomater. Sci.* **2025**, *13*, 3942–3957.

[8] Jin, Y.; Tan, A. L.; Feng, J.; Xu, Z. X.; Wang, P. W.; Ruan, P.; Luo, R. J.; Weng, Y. M.; Peng, M. Prognostic impact of memory CD8(+) T cells on immunotherapy in human cancers: A systematic review and meta-analysis. *Front. Oncol.* **2021**, *11*, 698076.

[9] Li, W. H.; Zhang, L. J. Rewiring mitochondrial metabolism for $CD8^+$ T cell memory formation and effective cancer immunotherapy. *Front. Immunol.* **2020**, *11*, 1834.

[10] Lv, B. Z.; Wang, Y. P.; Ma, D. J.; Cheng, W.; Liu, J.; Yong, T.; Chen, H.; Wang, C. Immunotherapy: Reshape the tumor immune microenvironment. *Front. Immunol.* **2022**, *13*, 844142.

[11] Wang, Q. Y.; Gao, Y.; Li, Q.; He, A.; Xu, Q. L.; Mou, Y. B. Enhancing dendritic cell activation through manganese-coated nanovaccine targeting the cGAS-STING pathway. *Int. J. Nanomed.* **2024**, *19*, 263–280.

[12] Bandara, S.; Raveendran, S. Current landscape and future directions in cancer immunotherapy: Therapies, trials, and challenges. *Cancers* **2025**, *17*, 821.

[13] Lu, J. S.; Li, Y.; Gao, X. H.; Chen, S. M.; Jin, Z. P.; Guo, X. X.; Xie, W. S.; Guo, Z. H.; Wei, Y.; Zhao, L. Y. DC-derived whole cell cytokine Nano-regulator for remodelling extracellular matrix and synergizing tumor immunotherapy. *RSC Med. Chem.* **2024**, *15*, 4090–4099.

[14] Chikovani, T.; Magen, E. *In situ* vaccination by tumor ablation: Principles and prospects for systemic antitumor immunity. *Vaccines* **2025**, *13*, 1114.

[15] Blee, C.; Muthana, M.; Wells, G.; Danson, S. Turning the tide: Harnessing vaccines and viruses to fight cancer. *Immunother. Adv.* **2025**, *5*, ltaf033.

[16] Li, J. Y.; Jiang, R. Y.; Wang, J.; Wang, X. J. Advances in mRNA vaccine therapy for breast cancer research. *Discov. Oncol.* **2025**, *16*, 673.

[17] Baharom, F.; Hermans, D.; Delamarre, L.; Seder, R. A. Vax-innate: Improving therapeutic cancer vaccines by modulating T cells and the tumour microenvironment. *Nat. Rev. Immunol.* **2025**, *25*, 195–211.

[18] Wu, Y. N.; Park, J.; Jin, D.; Lee, J.; Le, Q. V.; Oh, Y. K. Tannic acid-based nanomaterials for tolerogenic immunotherapy of rheumatoid arthritis. *Adv. Funct. Mater.* **2023**, *33*, 2305563.

[19] Chauhan, S. S.; Shetty, A. B.; Hatami, E.; Chowdhury, P.; Yallapu, M. M. Pectin-tannic acid Nano-complexes promote the delivery and bioactivity of drugs in pancreatic cancer cells. *Pharmaceutics* **2020**, *12*, 285.

[20] Abouelmagd, S. A.; Meng, F. F.; Kim, B. K.; Hyun, H.; Yeo, Y. Tannic acid-mediated surface functionalization of polymeric nanoparticles. *ACS Biomater. Sci. Eng.* **2016**, *2*, 2294–2303.

[21] Liu, M. Y.; Zhang, J. D.; Chen, S. N.; Zheng, J.; Xiao, L. L.; Liu, X. L.; Cao, Y.; Zhu, S. Y.; Chang, S. F. NIR-triggered metal-polyphenol nanoparticles enhance HPV-driven cancer immunotherapy via immunogenic cell death and STING sequential activation. *Adv. Healthc. Mater.* **2026**, *15*, e02884.

[22] Zhou, X.; Su, Q. H.; Zhao, H. W.; Cao, X. Y.; Yang, Y.; Xue, W. Metal-phenolic network-encapsulated nanovaccine with pH and reduction dual responsiveness for enhanced cancer immunotherapy. *Mol. Pharm.* **2020**, *17*, 4603–4615.

[23] Janes, M. E. Engineering translational vaccine delivery systems with the polyphenol tannic acid. Ph.D. Dissertation, Massachusetts Institute of Technology, Cambridge, MA, USA, 2024.

[24] Su, Q. H.; Liu, Z. W.; Du, R. L.; Chen, X. L.; Chen, L. L.; Fu, Z. M.; Luo, X. Y.; Yang, Y.; Shi, X. Q. Facile preparation of a metal-phenolic network-based lymph node targeting nanovaccine for antitumor immunotherapy. *Acta Biomater.* **2023**, *158*, 510–524.

[25] Chong, G. W.; Su, R. P.; Gu, J. J.; Yang, Y. S.; Zhang, T. T.; Zang, J.; Zhao, Y. G.; Zheng, X.; Liu, Y.; Ruan, S. R. et al. Catalytic nanovaccine for cancer immunotherapy: A NADPH oxidase-inspired Fe-polyphenol network nanovaccine for enhanced antigen cross-presentation. *Chem. Eng. J.* **2022**, *435*, 134993.

[26] Qiu, H. M.; Wang, S. M.; Huang, R. M.; Liu, X. Y.; Li, L. Q.; Liu, Z.; Wang, A. H.; Ji, S. C.; Liang, H.; Jiang, B. P. et al. Acidity-responsive polyphenol-coordinated nanovaccines for improving tumor immunotherapy via bidirectional reshaping of the immunosuppressive microenvironment and controllable release of antigens. *Biomater. Sci.* **2024**, *12*, 3175–3192.

[27] Guo, Z. H.; Xie, W. S.; Lu, J. S.; Guo, X. X.; Xu, J. Z.; Xu, W. L.; Chi, Y. J.; Takuya, N.; Wu, H.; Zhao, L. Y. Tannic acid-based metal phenolic networks for bio-applications: A review. *J. Mater. Chem. B* **2021**, *9*, 4098–4110.

[28] Shin, M.; Park, E.; Lee, H. Plant-inspired pyrogallol-containing functional materials. *Adv. Funct. Mater.* **2019**, *29*, 1903022.

[29] Ren, Z. M.; Zhang, Y. L.; Liu, Y. Y.; Wang, G. *In situ* antibiotic-loaded copper tannic acid coordination nanospheres targeting biofilms for the treatment of chronic osteomyelitis. *Int. J. Nanomed.* **2025**, *20*, 13641–13659.

[30] Han, L. L.; Liu, Q.; Yang, L. W.; Ye, T.; He, Z. F.; Jia, L. Y. Facile oriented immobilization of histidine-tagged proteins on nonfouling cobalt polyphenolic self-assembly surfaces. *ACS Biomater. Sci. Eng.* **2017**, *3*, 3328–3337.

[31] Lu, J. S.; Guo, Z. H.; Chen, S. M.; Li, Y.; Xu, X.; Yu, J.; Che, S. L.; Zhang, G. F.; Xie, W. S.; Wei, Y. et al. Investigation of the impact of local tumor phenolic-chemistry for dual starvation and vaccination therapy. *Chem. Eng. J.* **2025**, *524*, 169504.

[32] Pires, F. Q.; Alves-Silva, I.; Pinho, L. A. G.; Chaker, J. A.; Sa-Barreto, L. L.; Gelfuso, G. M.; Gratieri, T.; Cunha-Filho, M. Predictive models of FDM 3D printing using experimental design based on pharmaceutical requirements for tablet production. *Int. J. Pharm.* **2020**, *588*, 119728.

[33] Ran, Y. L.; Hu, J. F.; Chen, Y. Y.; Rao, Z. N.; Zhao, J. C.; Xu, Z. G.; Ming, J. Morusin-Cu(II)-indocyanine green nanoassembly ignites mitochondrial dysfunction for chemo-photothermal tumor therapy. *J. Colloid Interface Sci.* **2024**, *662*, 760–773.

[34] Yan, F.; Wu, H.; Liu, H.M.; Deng, Z.T.; Liu, H.; Duan, W.L.; Liu, X.; Zheng, H.R. Molecular imaging-guided photothermal/photodynamic therapy against tumor by iRGD-modified indocyanine green nanoparticles. *J. Controlled Release* **2016**, *224*, 217–228.

[35] Zhao, P. F.; Zheng, M. B.; Yue, C. X.; Luo, Z. Y.; Gong, P.; Gao, G. H.; Sheng, Z. H.; Zheng, C. F.; Cai, L. T. Improving drug accumulation and photothermal efficacy in tumor depending on size of ICG loaded lipid-polymer nanoparticles. *Biomaterials* **2014**, *35*, 6037–6046.

[36] Zheng, Y. Y.; Xie, Y. Y.; Dong, X.; Shen, S. L.; Zheng, G. S.; Weng, J. Q.; Yan, Q. Y. ICG@ZIF@HA nanoparticles and GO-loaded freeze-drying microneedles mediated PDT/PTT dual-modal phototherapeutic for efficient bacterial biofilm elimination. *ACS Appl. Polym. Mater.* **2025**, *7*, 11012–11026.

[37] Amiri, H.; Bordonali, L.; Lascialfari, A.; Wan, S.; Monopoli, M. P.; Lynch, I.; Laurent, S.; Mahmoudi, M. Protein corona affects the relaxivity and MRI contrast efficiency of magnetic nanoparticles. *Nanoscale* **2013**, *5*, 8656–8665.

[38] Xu, T.; Yang, X. P.; Chen, X. Y.; Wang, Q. L.; Ye, J. C.; You, C. Y.; Zhu, J.; Gui, Y. Emerging photothermal agents combined with immunotherapy for cancer treatment. *Discov. Oncol.* **2025**, *16*, 1936.

[39] Talukdar, P.; Winegar, P. H.; Hudson, G. A.; Astolfi, M. C. T.; Inman, J. L.; Keasling, J. D.; Mukundan, H. From bark to bench: Innovations in QS-21 adjuvant characterization and manufacturing. *Front. Immunol.* **2025**, *16*, 1677995.

[40] Welsby, I.; Detienne, S.; N'Kuli, F.; Thomas, S.; Wouters, S.; Bechtold, V.; De Wit, D.; Gineste, R.; Reinheckel, T.; Elouahabi, A. et al. Lysosome-dependent activation of human dendritic cells by the vaccine adjuvant QS-21. *Front. Immunol.* **2016**, *7*, 663.